

Generalized Allen–Cahn-type phase-field crystal model with FCC ordering structure and its conservative high-order accurate algorithm

Zhijun Tan ^{a,b}, Le Chen ^a, Junxiang Yang ^{a,*}

^a School of Computer Science and Engineering, Sun Yat-sen University, Guangzhou 510006, China

^b Guangdong Province Key Laboratory of Computational Science, Sun Yat-sen University, Guangzhou 510275, China



ARTICLE INFO

Article history:

Received 25 October 2022

Received in revised form 19 December 2022

Accepted 3 January 2023

Available online 5 January 2023

Keywords:

Phase-field crystal model

FCC ordering structure

Conservative algorithm

High-order accuracy

ABSTRACT

In this paper, a generalized Allen–Cahn-type phase-field crystal model with face-centered-cubic ordering structure is presented. By introducing a space-time dependent Lagrange multiplier, the mass conservation is enforced and the local effect can be reflected. Moreover, the proposed model is lower-order in space and will be more efficient for numerical computation. For the simulation of crystallization, the main challenge is to design practical and stable algorithm which meanwhile guarantees the high-order accuracy. To resolve this problem, we propose a temporally high-order (up to third-order) accurate and linear multi-stage scheme based on implicit-explicit Runge–Kutta approach. The nonlinear term is explicitly treated and the appropriate stabilizer is added to balance the stiffness. By utilizing the Fourier spectral method in space, the numerical calculation is easy to implement. We analytically proved the discrete mass conservation property based on the fully discrete scheme. Extensive numerical experiments are performed to validate the accuracy, efficiency, and capability for phase transition. The effects of parameters and local interaction are investigated in detail. To facilitate the interested readers, we provide MATLAB codes of our proposed method in Appendix A.

© 2023 Elsevier B.V. All rights reserved.

1. Introduction

In the natural and industrial fields, the crystallization usually occurs in the supercooled liquid solution. During this process, the phase transition from liquid to solid leads to the formation of closely arranged crystal structures. Under the effects of material properties and environmental temperature, different crystallization phenomena will be observed, such as body-centered-cubic (BCC) patterns [1–3], face-centered-cubic (FCC) patterns [4], square crystal [5,6], anisotropic structures [7], and quasicrystal [8,9], etc. In recent years, the phase-field method is practical and popular to model physical problems with interface and density field, see [10–14] for successful applications. For the crystallization, the well-known molecular dynamics method is effective, but is generally time consuming because the motion of each molecule should be computed. The phase-field method is another popular approach in computational material sciences, which introduces an order parameter (phase-field function) to represent the temporal average of atomic density. The phase-field method links the elasticity in atomic scale and the phase transition in macroscopic level. The computation is more efficient because we only need to update the phase-field function instead of each molecule. Based on phase-field theory, Elder et al. [15] originally investigated the crystallization with BCC ordering structure. The specific form of free energy functional is constructed to reflect different dynamics of crystal growth. By taking the variational derivative of free energy to phase-field function and considering a particular gradient flow approach, the evolutional equations are derived. By utilizing the H^{-1} -gradient flow, we obtain the Cahn–Hilliard (CH)-type phase-field crystal (PFC) model which naturally satisfies the mass conservation law if we consider the periodic case. To investigate the PFC model with BCC ordering, Wise et al. [16] developed a first-order time-accurate and unconditionally stable nonlinear scheme. To accelerate the convergence, Hu et al. [17] utilized the finite difference based nonlinear multigrid algorithm to solve the same PFC model. Based on the convex splitting approach, Wang and Wise [18] proposed an energy-stable and convergent method for the modified PFC model. For the modified PFC equation, Baskaran et al. [19] developed an energy-stable nonlinear finite difference method and they utilized the multigrid technique to accelerate

* The review of this paper was arranged by Prof. David W. Walker.

* Corresponding author.

E-mail address: yangjx79@mail.sysu.edu.cn (J. Yang).

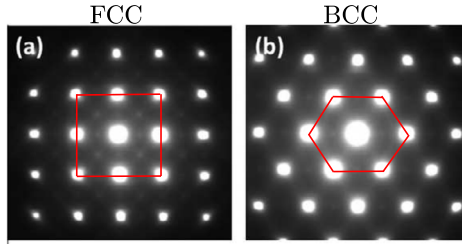


Fig. 1. Experimental observations of FCC ordering (left) and BCC ordering (right) of CoCrCuFeNiAl_{0.5} alloy. The results are adapted from [37] with the permission of Elsevier.

the computation. Later, Baskaran et al. [20] performed detailed convergence analysis of a nonlinear convex splitting method for the modified PFC equation. Based on the Fourier pseudo-spectral method in space, Cheng et al. [21] presented an energy-stable algorithm for the square PFC model. The numerical simulation and detailed convergence analysis for the three-dimensional PFC model with BCC ordering was reported in [22]. Based on the recently developed operator splitting, new convex splitting, linear stabilization, and auxiliary variable approaches, typical researches related to the CH-type PFC model with BCC ordering structure and various variants can be found in [23–28] and references therein. If we derive the equation based on the L^2 -gradient flow and consider the same free energy of classical PFC model [16], the well-known Swift–Hohenberg (SH) model describing the pattern formation in Rayleigh–Benard convection [29] can be obtained. See [30–32] for some numerical investigations on the SH model. Unfortunately, the Allen–Cahn (AC)-type PFC model (i.e., SH model) can not preserve the total mass. To simulate the mass-conserved crystallization by using a AC-type model, a popular approach is to introduce a Lagrange multiplier. Many previous works [33–36] pointed out that the mass-conserved AC-type PFC model achieved similar results of the classical CH-type PFC model. Comparing with the AC-type PFC model, the CH-type PFC model includes higher order derivative in space and this will leads to more tough stability condition on numerical computation. Moreover, extra computation of spatial derivative also increases the computational costs.

By introducing the two-mode effect, the quadrilateral FCC patterns can be observed in experiments. Fig. 1 shows the experimental results of BCC ordering alloy (right) and FCC ordering alloy (left) [37]. Based on phase-field method, Wu et al. [4] developed two-mode PFC model for describing the FCC ordering structure. Comparing with the classical PFC model with BCC ordering [16,23,27,28], the CH-type PFC model with FCC ordering leads to more challenges in numerical computation because this model is tenth-order in space. It is worth noting that the order in space means the number of spatial derivatives. For example, the Laplacian operator Δ is second-order in space. From Eqs. (3) and (4) in the next section, it is easy to check that the CH-type PFC model with FCC ordering is tenth-order. If $L_2 \equiv 1$ and $\xi \equiv 0$, Eqs. (3) and (4) degenerate to the CH-type PFC model with BCC ordering, it is obvious that this model is sixth-order. By adopting the auxiliary variable method in time and Fourier spectral method in space, Zhang and Yang [38] developed a linear, second-order time-accurate, and stable scheme to numerically investigate the dynamics of CH-type PFC model with FCC ordering. To simplify the computation, Li et al. [39] recently designed a eighth-order PFC model with FCC ordering based on the AC-type gradient flow.

In [39], authors adopted a global Lagrange multiplier to enforce the mass conservation and performed the simulations with a temporally second-order accurate scheme. Actually, the global Lagrange multiplier can not reflect the effect of local information. Moreover, long-time simulation of phase transition requires the higher-order accuracy of algorithm. To resolve these, we first develop a generalized mass-conserved PFC model with FCC ordering structure based on the L^2 -gradient flow. A space-time dependent Lagrange multiplier is introduced to preserve the total mass and impose the local effect. By utilizing the implicit-explicit Runge–Kutta (IMEX RK) approach, we develop a third-order four-stage temporal scheme in which the nonlinear term is explicitly treated and a stabilization technique is applied. The governing equation is discretized in space by using the Fourier spectral method. In each time step, the proposed method is linear and efficient. The analytical estimation shows that the proposed fully discrete scheme strictly satisfies the discrete version of mass conservation. To our best knowledge, this is the first work focusing on a generalized AC-type PFC model with FCC ordering structure and its mass-conserved high-order (up to third-order) accurate computation.

The rest sections are organized as follows. We briefly review the mass-conserved PFC models with FCC ordering structure based on H^{-1} - and L^2 -gradient flows and then present the proposed generalized AC-type model in Section 2. Based on the implicit-explicit Runge–Kutta approach, the conservative high-order (up to third order) accurate algorithm is developed in Section 3. Extensive numerical experiments are performed in Section 4. In Section 5, the conclusions are drawn. The MATLAB codes are given in Appendix A.

2. Generalized AC-type PFC model

In domain Ω , the local atomic density is described by a phase-field function $\phi = \phi(\mathbf{x}, t)$, where \mathbf{x} is the spatial variables and $t \geq 0$ is the temporal variable. The free energy functional for the PFC model with FCC ordering structure reads as [38,39]

$$E(\phi) = \int_{\Omega} \left(\frac{\phi}{2} L_1^2 (L_2^2 + \xi^2) \phi + F(\phi) \right) d\mathbf{x}, \quad (1)$$

where $L_1 = \Delta + 1$ and $L_2 = \Delta + \eta^2$ are linear operators, Δ is the Laplacian operator, the nonlinear potential is $F(\phi) = 0.25\phi^4 - 0.5\epsilon\phi^2$, ξ , η , and ϵ are non-negative constants which are related to specific physical phenomena. It is worth noting that the above energy functional can be used to describe the classical PFC dynamics with BCC ordering structure [16] if we set $L_2 \equiv 1$ and $\xi \equiv 0$. By taking the variational approach to Eq. (1), the following chemical potential is obtained

$$\mu = \frac{\delta E(\phi)}{\delta \phi} = L_1^2 (L_2^2 + \xi^2) \phi + F'(\phi), \quad (2)$$

where $F'(\phi) = \phi^3 - \epsilon\phi$. Based on the H^{-1} -gradient flow, the governing equations of CH-type PFC model with FCC ordering structure are postulated as [38]

$$\frac{\partial \phi}{\partial t} = \Delta\mu, \quad (3)$$

$$\mu = \frac{\delta E(\phi)}{\delta \phi} = L_1^2(L_2^2 + \xi^2)\phi + F'(\phi). \quad (4)$$

During the phase transition from liquid to solid crystals, the mass conservation is a basic property. Therefore, the physically consistent PFC model should also satisfy the mass-conserved property. By taking the time derivative to the integral of ϕ over Ω , we have

$$\frac{d}{dt} \int_{\Omega} \phi \, d\mathbf{x} = \int_{\Omega} \frac{\partial \phi}{\partial t} \, d\mathbf{x} = \int_{\Omega} \Delta\mu \, d\mathbf{x} = \int_{\partial\Omega} \nabla\mu \cdot \mathbf{n} \, ds = 0, \quad (5)$$

where Eq. (3) and divergence theorem are used, $\partial\Omega$ is the domain boundary, \mathbf{n} is the unit normal vector to $\partial\Omega$. On $\partial\Omega$, the periodic boundary condition is considered. The above equality indicates that the H^{-1} -gradient flow based PFC model with FCC ordering structure satisfies the mass conservation. We notice that the tenth-order PFC model includes higher order spatial derivative (i.e., the Laplacian operator is introduced into the left-hand side of Eq. (3)) and this will leads to numerical problems related to efficiency.

To fix this shortcoming and maintain the mass conservation, Li et al. [39] recently developed a AC-type PFC model with FCC ordering structure. Based on the L^2 -gradient flow (i.e., $\frac{\partial \phi}{\partial t} = -\mu$), the governing equation reads as

$$\frac{\partial \phi}{\partial t} = -L_1^2(L_2^2 + \xi^2)\phi - F'(\phi) + \frac{1}{|\Omega|} \int_{\Omega} ((\eta^4 + \xi^2)\phi + F'(\phi)) \, d\mathbf{x}, \quad (6)$$

where the last term is the time-dependent (nonlocal) Lagrange multiplier which enforces the mass conservation, $|\Omega|$ is the area of domain. It can be observed that the above model is eighth-order and the computation will be more efficient. To show the mass conservation, we take the time derivative to the integral of ϕ over Ω and get

$$\frac{d}{dt} \int_{\Omega} \phi \, d\mathbf{x} = \int_{\Omega} \frac{\partial \phi}{\partial t} \, d\mathbf{x} = \int_{\Omega} \left[-L_1^2(L_2^2 + \xi^2)\phi - F'(\phi) + \frac{1}{|\Omega|} \int_{\Omega} ((\eta^4 + \xi^2)\phi + F'(\phi)) \, d\mathbf{x} \right] \, d\mathbf{x} = 0. \quad (7)$$

The recently developed mass-conserved AC-type PFC model [39] only considers a nonlocal Lagrange multiplier to preserve the mass. In fact, the mass conservation can also be satisfied by imposing space-time dependent (local) Lagrange multiplier. For the mass-conserved AC model, the previous researches [40,41] pointed out that the space-time dependent Lagrange multiplier led to slightly different dynamics because the local information was considered. Based on the similar idea for the AC equation, a generalized conservative PFC model with FCC ordering structure is proposed to be

$$\frac{\partial \phi}{\partial t} = -L_1^2(L_2^2 + \xi^2)\phi - F'(\phi) + (I(\phi))^r \beta(t), \quad (8)$$

where $(I(\phi))^r \beta(t)$ is the space-time dependent Lagrange multiplier, $I(\phi) = \frac{\eta^4 + \xi^2}{2}\phi^2 + F(\phi)$ and $\beta(t) = \frac{\int_{\Omega} I'(\phi) \, d\mathbf{x}}{\int_{\Omega} (I(\phi))^r \, d\mathbf{x}}$. As $r = 0$, our proposed model becomes the AC-type PFC model in [39]. Comparing with the nonlocal model, the present model not only has generalized formulation but also can include the local effect. By taking the time derivative to the integral of ϕ over Ω , we get

$$\begin{aligned} \frac{d}{dt} \int_{\Omega} \phi \, d\mathbf{x} &= \int_{\Omega} \frac{\partial \phi}{\partial t} \, d\mathbf{x} = \int_{\Omega} \left[-L_1^2(L_2^2 + \xi^2)\phi - F'(\phi) + (I(\phi))^r \beta(t) \right] \, d\mathbf{x} \\ &= - \int_{\Omega} I'(\phi) \, d\mathbf{x} + \beta(t) \int_{\Omega} (I(\phi))^r \, d\mathbf{x} = - \int_{\Omega} I'(\phi) \, d\mathbf{x} + \frac{\int_{\Omega} I'(\phi) \, d\mathbf{x}}{\int_{\Omega} (I(\phi))^r \, d\mathbf{x}} \int_{\Omega} (I(\phi))^r \, d\mathbf{x} = 0. \end{aligned} \quad (9)$$

The above equality indicates that the proposed generalized model satisfies the property of mass conservation. In the next section, we will develop the linear and temporally high-order (up to third-order) accurate algorithm for the proposed model. By considering the periodic condition, the spatial discretization will be performed based on Fourier spectral method [42,43].

3. Conservative high-order accurate algorithm

For the convenience of explanation, we herein discretize the proposed model in two-dimensional (2D) domain $\Omega = [0, L_x] \times [0, L_y]$. The uniform space step is defined as $h = L_x/N_x = L_y/N_y$, where N_x and N_y are positive integers. The grid point is defined as $(x_m, y_n) = (mh, nh)$, where $m = 0, 1, \dots, N_x - 1$ and $n = 0, 1, \dots, N_y - 1$. Let $\Delta t = T/N_t$ be the uniform time step, where T is the total computational time and N_t is the number of time iteration. The numerical approximation of $\phi(x_m, y_n, k\Delta t)$ is ϕ_{mn}^k and the superscript represents k -th time level. The discrete Fourier transform and its inverse version are defined to be [42,43]

$$\hat{\phi}_{pq}^k = \sum_{m=0}^{N_x-1} \sum_{n=0}^{N_y-1} \phi_{mn}^k e^{-i(\xi_p x_m + \eta_q y_n)}, \quad (10)$$

$$\phi_{mn}^k = \frac{1}{N_x N_y} \sum_{p=0}^{N_x-1} \sum_{q=0}^{N_y-1} \hat{\phi}_{pq}^k e^{i(\xi_p x_m + \eta_q y_n)}, \quad (11)$$

where $\xi_p = 2\pi p/L_x$ and $\eta_q = 2\pi q/L_y$. From [42,43], the discrete Laplacian term is recast to be

$$\Delta \phi_{mn}^k = -\frac{1}{N_x N_y} \sum_{p=0}^{N_x-1} \sum_{q=0}^{N_y-1} (\xi_p^2 + \eta_q^2) \hat{\phi}_{pq}^k e^{i(\xi_p x_m + \eta_q y_n)}. \quad (12)$$

The high-order spatial terms, such as $\Delta^2 \phi_{mn}^k$, $\Delta^3 \phi_{mn}^k$, and $\Delta^4 \phi_{mn}^k$, can be similarly defined. To construct linear scheme, we first recast Eq. (8) to be the following equivalent form

$$\begin{aligned} \frac{\partial \phi}{\partial t} &= -L_1^2 (L_2^2 + \xi^2) \phi - F'(\phi) + (I(\phi))^r \beta(t) - S(\phi - \phi) \\ &= -\left(\Delta^4 \phi + (2\eta^2 + 2)\Delta^3 \phi + (\eta^4 + 4\eta^2 + \xi^2)\Delta^2 \phi + (2\eta^4 + 2\eta^2 + 2\xi^2)\Delta \phi \right) - (\eta^4 + \xi^2)\phi \\ &\quad - F'(\phi) + (I(\phi))^r \beta(t) - S(\phi - \phi). \end{aligned} \quad (13)$$

Then we treat $-(S\phi + \Delta^4 \phi + (2\eta^2 + 2)\Delta^3 \phi + (\eta^4 + 4\eta^2 + \xi^2)\Delta^2 \phi + (2\eta^4 + 2\eta^2 + 2\xi^2)\Delta \phi)$ in an implicit manner and treat $-(\eta^4 + \xi^2)\phi - F'(\phi) + (I(\phi))^r \beta(t) + S\phi$ in an explicit manner. Here, $S > 0$ is a stabilization constant. For convenience, we let

$$\begin{aligned} H(\phi) &= -\left(S\phi + \Delta^4 \phi + (2\eta^2 + 2)\Delta^3 \phi + (\eta^4 + 4\eta^2 + \xi^2)\Delta^2 \phi + (2\eta^4 + 2\eta^2 + 2\xi^2)\Delta \phi \right), \\ Q(\phi) &= -(\eta^4 + \xi^2)\phi - F'(\phi) + (I(\phi))^r \beta(t) + S\phi. \end{aligned}$$

Based on the third-order four-stage IMEX RK approach [44], the fully discrete scheme for solving Eq. (13) is

$$\phi_{mn}^{(1)} = \phi_{mn}^k + \Delta t \left(\frac{1}{2} H(\phi_{mn}^{(1)}) + \frac{1}{2} Q(\phi_{mn}^k) \right), \quad (14)$$

$$\phi_{mn}^{(2)} = \phi_{mn}^k + \Delta t \left(\frac{1}{2} H(\phi_{mn}^{(2)}) + \frac{1}{6} H(\phi_{mn}^{(1)}) + \frac{1}{18} Q(\phi_{mn}^{(1)}) + \frac{11}{18} Q(\phi_{mn}^k) \right), \quad (15)$$

$$\begin{aligned} \phi_{mn}^{(3)} &= \phi_{mn}^k + \Delta t \left(\frac{1}{2} H(\phi_{mn}^{(3)})_{mn} + \frac{1}{2} H(\phi_{mn}^{(2)}) - \frac{1}{2} H(\phi_{mn}^{(1)}) \right. \\ &\quad \left. + \frac{1}{2} Q(\phi_{mn}^{(2)}) - \frac{5}{6} Q(\phi_{mn}^{(1)}) + \frac{5}{6} Q(\phi_{mn}^k) \right), \end{aligned} \quad (16)$$

$$\begin{aligned} \phi_{mn}^{k+1} &= \phi_{mn}^k + \Delta t \left(\frac{1}{2} H(\phi_{mn}^{k+1}) + \frac{1}{2} H(\phi_{mn}^{(3)}) - \frac{3}{2} H(\phi_{mn}^{(2)}) + \frac{3}{2} H(\phi_{mn}^{(1)}) \right. \\ &\quad \left. - \frac{7}{4} Q(\phi_{mn}^{(3)}) + \frac{3}{4} Q(\phi_{mn}^{(2)}) + \frac{7}{4} Q(\phi_{mn}^{(1)}) + \frac{1}{4} Q(\phi_{mn}^k) \right). \end{aligned} \quad (17)$$

The above scheme is named as RK-3. In each time step, we successively solve Eqs. (14)–(17). The computation is easy to implement because all equations are linear decoupled and equipped with constant coefficients. In the following contents, the implementation of algorithm will be summarized. Moreover, the discrete version of mass conservation will be proved.

Implementation: By transforming Eq. (14) into discrete Fourier space, we have

$$\hat{\phi}_{pq}^{(1)} = \frac{\hat{\phi}_{pq}^k + \frac{\Delta t}{2} \hat{Q}_{pq}^k}{1 + \frac{\Delta t}{2} C_f}, \quad (18)$$

where $C_f = (S - (2\eta^4 + 2\eta^2 + 2\xi^2)(\xi_p^2 + \eta_q^2) + (\eta^4 + 4\eta^2 + \xi^2)(\xi_p^2 + \eta_q^2)^2 - (2\eta^2 + 2)(\xi_p^2 + \eta_q^2)^3 + (\xi_p^2 + \eta_q^2)^4)$, $\hat{Q}_{pq}^k = \mathcal{F}[Q(\phi_{mn}^k)]$ and \mathcal{F} represents the discrete Fourier transform. With computed $\hat{\phi}_{pq}^{(1)}$ from Eq. (18), the solution in physical space (i.e., $\phi_{mn}^{(1)}$) can be recovered by using the discrete Fourier inverse transform (i.e., Eq. (11)). The similar procedures are used to calculate $\phi_{mn}^{(2)}$, $\phi_{mn}^{(3)}$, and ϕ_{mn}^{k+1} because these equations have same structure (i.e., linear elliptic type equations with constant coefficients). With computed ϕ_{mn}^{k+1} , the calculations in next time step can be conducted.

Discrete mass conservation: To show the discrete mass conservation (i.e., $\sum_{m=0}^{N_x-1} \sum_{n=0}^{N_y-1} \phi_{mn}^{k+1} = \sum_{m=0}^{N_x-1} \sum_{n=0}^{N_y-1} \phi_{mn}^k$ for $k = 0, 1, 2, \dots$), we successively prove $\sum_{m=0}^{N_x-1} \sum_{n=0}^{N_y-1} \phi_{mn}^{(1)} = \sum_{m=0}^{N_x-1} \sum_{n=0}^{N_y-1} \phi_{mn}^k$, $\sum_{m=0}^{N_x-1} \sum_{n=0}^{N_y-1} \phi_{mn}^{(2)} = \sum_{m=0}^{N_x-1} \sum_{n=0}^{N_y-1} \phi_{mn}^{(1)}$, $\sum_{m=0}^{N_x-1} \sum_{n=0}^{N_y-1} \phi_{mn}^{(3)} = \sum_{m=0}^{N_x-1} \sum_{n=0}^{N_y-1} \phi_{mn}^{(2)}$, and $\sum_{m=0}^{N_x-1} \sum_{n=0}^{N_y-1} \phi_{mn}^{k+1} = \sum_{m=0}^{N_x-1} \sum_{n=0}^{N_y-1} \phi_{mn}^{(3)}$. From Eq. (18), we have

$$\sum_{m=0}^{N_x-1} \sum_{n=0}^{N_y-1} \phi_{mn}^{(1)} = \hat{\phi}_{00}^{(1)} = \frac{\hat{\phi}_{00}^k + \Delta t \hat{Q}_{00}^k / 2}{1 + S \Delta t / 2} = \frac{\hat{\phi}_{00}^k + S \Delta t \hat{\phi}_{00}^k / 2}{1 + S \Delta t / 2} = \hat{\phi}_{00}^k = \sum_{m=0}^{N_x-1} \sum_{n=0}^{N_y-1} \phi_{mn}^k, \quad (19)$$

where

$$\begin{aligned}\hat{Q}_{00}^k &= \sum_{m=0}^{N_x-1} \sum_{n=0}^{N_y-1} Q(\phi_{mn}^k) = - \sum_{m=0}^{N_x-1} \sum_{n=0}^{N_y-1} ((\eta^4 + \xi^2)\phi_{mn}^k + F'(\phi_{mn}^k) - S\phi_{mn}^k) + \beta^k \sum_{m=0}^{N_x-1} \sum_{n=0}^{N_y-1} (I(\phi_{mn}^k))^r \\ &= - \sum_{m=0}^{N_x-1} \sum_{n=0}^{N_y-1} ((\eta^4 + \xi^2)\phi_{mn}^k + F'(\phi_{mn}^k) - S\phi_{mn}^k) + \frac{\sum_{m=0}^{N_x-1} \sum_{n=0}^{N_y-1} I'(\phi_{mn}^k)}{\sum_{m=0}^{N_x-1} \sum_{n=0}^{N_y-1} (I(\phi_{mn}^k))^r} \sum_{m=0}^{N_x-1} \sum_{n=0}^{N_y-1} (I(\phi_{mn}^k))^r \\ &= S \sum_{m=0}^{N_x-1} \sum_{n=0}^{N_y-1} \phi_{mn}^k = S\hat{\phi}_{00}^k.\end{aligned}$$

By transforming Eqs. (15) to discrete Fourier space and using the similar treatment, we can prove

$$\sum_{m=0}^{N_x-1} \sum_{n=0}^{N_y-1} \phi_{mn}^{(2)} = \hat{\phi}_{00}^{(2)} = \frac{\hat{\phi}_{00}^k + \Delta t \left(-\frac{S}{6}\hat{\phi}_{00}^{(1)} + \frac{S}{18}\hat{\phi}_{00}^{(1)} + \frac{11S}{18}\hat{\phi}_{00}^k \right)}{1 + \Delta t S/2} = \hat{\phi}_{00}^{(1)} = \sum_{m=0}^{N_x-1} \sum_{n=0}^{N_y-1} \phi_{mn}^{(1)}. \quad (20)$$

By transforming Eqs. (16) to discrete Fourier space and using the similar treatment, we get

$$\begin{aligned}\sum_{m=0}^{N_x-1} \sum_{n=0}^{N_y-1} \phi_{mn}^{(3)} &= \hat{\phi}_{00}^{(3)} = \frac{\hat{\phi}_{00}^k + \Delta t \left(-\frac{S}{2}\hat{\phi}_{00}^{(2)} + \frac{S}{2}\hat{\phi}_{00}^{(1)} + \frac{S}{2}\hat{\phi}_{00}^{(2)} - \frac{5S}{6}\hat{\phi}_{00}^{(1)} + \frac{5S}{6}\hat{\phi}_{00}^k \right)}{1 + \Delta t S/2} \\ &= \hat{\phi}_{00}^{(2)} = \sum_{m=0}^{N_x-1} \sum_{n=0}^{N_y-1} \phi_{mn}^{(2)}.\end{aligned} \quad (21)$$

Note that the above results indicate $\hat{\phi}_{00}^{(3)} = \hat{\phi}_{00}^{(2)} = \hat{\phi}_{00}^{(1)} = \hat{\phi}_{00}^k$. By transforming Eq. (17) to discrete Fourier space, we finally obtain

$$\begin{aligned}\sum_{m=0}^{N_x-1} \sum_{n=0}^{N_y-1} \phi_{mn}^{k+1} &= \hat{\phi}_{00}^{k+1} = \frac{\hat{\phi}_{00}^k + \Delta t \left(-\frac{S}{2}\hat{\phi}_{00}^{(3)} + \frac{3S}{2}\hat{\phi}_{00}^{(2)} - \frac{3S}{2}\hat{\phi}_{00}^{(1)} - \frac{7}{4}\hat{Q}_{00}^{(3)} + \frac{3}{4}\hat{Q}_{00}^{(2)} + \frac{7}{4}\hat{Q}_{00}^{(1)} + \frac{1}{4}\hat{Q}_{00}^k \right)}{1 + S\Delta t/2} \\ &= \hat{\phi}_{00}^k = \sum_{m=0}^{N_x-1} \sum_{n=0}^{N_y-1} \phi_{mn}^k.\end{aligned} \quad (22)$$

The proof of discrete mass conservation of RK-3 scheme is completed.

Remark 3.1. In this section, we present a temporally third-order accurate scheme based on the IMEX RK approach. In each time step, the proposed algorithm is linear and decoupled. We only need to successively solve four linear elliptic type equations with constant coefficients. By utilizing the Fourier spectral method in space, the numerical implementation is highly efficient. To facilitate the interested readers, we also present the temporally first-order accurate and second-order accurate schemes based on low-order RK as follows

$$\text{RK-1 : } \phi_{mn}^{k+1} = \phi_{mn}^k + \Delta t \left(H(\phi_{mn}^{k+1}) + Q(\phi_{mn}^k) \right), \quad (23)$$

$$\text{RK-2 : } \phi_{mn}^{(1)} = \phi_{mn}^k + \Delta t \left(\frac{2-\sqrt{2}}{2} H(\phi_{mn}^{(1)}) + \frac{2-\sqrt{2}}{2} Q(\phi_{mn}^k) \right), \quad (24)$$

$$\phi_{mn}^{k+1} = \phi_{mn}^k + \Delta t \left(\frac{2-\sqrt{2}}{2} H(\phi_{mn}^{k+1}) + \frac{\sqrt{2}}{2} H(\phi_{mn}^{(1)}) + \frac{1}{2-\sqrt{2}} Q(\phi_{mn}^{(1)}) + \frac{1-\sqrt{2}}{2-\sqrt{2}} Q(\phi_{mn}^k) \right). \quad (25)$$

For the choices of parameters, see [44] and references therein.

Remark 3.2. The generalized AC-type PFC model includes a space-time dependent Lagrange multiplier, this local term leads to some difficulties to analytically obtain energy dissipation law. Therefore, it is generally hard for us to design energy-stable scheme for the present model. In our upcoming works, the error and convergence estimations of our proposed method will be further considered.

4. Numerical experiments

In this section, we perform numerical simulations to verify the proposed method. The phase-field variable ϕ is assumed to be periodic. In subsection 4.1, the accuracy and efficiency are validated. In subsection 4.2, we perform a long-time simulation of phase transition with FCC ordering structure. The effects of parameters and initial setting will be investigated in the rest subsections. Unless otherwise specified, $S = 2$, $\eta = \sqrt{2}$, and $r = 0$ are used.

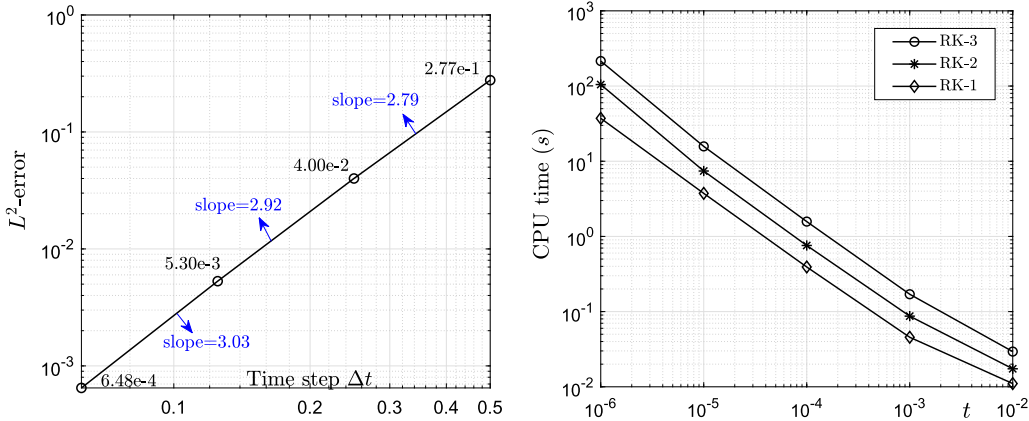


Fig. 2. L^2 -errors and CPU costs are shown in the left and right figures, respectively. The temporal accuracy is third order and the relation between CPU cost and time step is approximately linear.

4.1. Accuracy and efficiency tests

First of all, the temporal accuracy of our proposed third-order RK scheme is investigated. The computational domain is defined as $\Omega = [0, 32]$. The initial state is $\phi(x, 0) = \sin(\pi x/16)$. The space step is set to be $h = 1/3$. Other parameters are $\epsilon = 0.195$, $\xi = 0$, and $S = 0$. The simulations are performed by using $\Delta t = 2^{-1}, 2^{-2}, 2^{-3}, 2^{-4}$ and the reference solution is obtained by using $\Delta t = 2^{-12}$. The L^2 -error is calculated by the comparison with reference solution. The left of Fig. 2 shows the L^2 -errors and convergence rates under different time steps in log scale. The results indicate that the proposed algorithm achieves third-order accuracy in time.

We note that the proposed third-order accurate algorithm is a four-stage scheme. Although four linear equations should be successively solved in each time step, all of them are linear elliptic type equations with constant coefficients. Therefore, the CPU costs should be linear with respect to time step. To confirm this, we list the CPU times (in second) with different time steps in the right of Fig. 2. To perform quantitative comparison, the CPU costs for the temporally first-order accurate RK and second-order RK are also plotted. All simulations are performed on a standard laptop with an Intel 1.6 GHz CPU. The linear relationship can be observed. Comparing with the first- and second-order schemes, the CPU cost of the third-order RK scheme is endurable.

4.2. Long-time simulation of phase transition

For the uniformly distributed mixtures, the small perturbation on the system will lead to the start of phase transition. Finally, the dotted crystal patterns with FCC ordering structure occupy the whole domain. To simulate this, we consider the initial condition as $\phi(x, y, 0) = 0.23 + 0.01\text{rand}(x, y)$ in $\Omega = [0, 256] \times [0, 256]$, where $\text{rand}(x, y)$ is the random number between -1 and 1 . We set $\Delta t = 0.1$, $h = 1$, $\epsilon = 0.195$, and $\xi = 0.01$. The computation is performed until $t = 2000$ which is a relatively long time to reach numerical equilibrium state. The snapshots (a)-(f) in Fig. 3 show the results at different moments. We observe that the dotted patterns with FCC ordering structure gradually occupy the whole domain. In Fig. 3(g), the evolution of normalized energy (i.e., E^n/E^0) is plotted. The curve is shown from the second set of data and E^0 represents the energy corresponding to the second set of data. Although the energy dissipation law of our proposed algorithm is not analytically proved. The numerical result indicates that the energy is still non-increasing in time. The result in Fig. 3(h) indicates that the mass is conserved. In Fig. 4, the final stage and its local close-up view are shown. Due to the FCC ordering structure, the obvious grain boundaries (defects) appears.

4.3. Effects of ϵ and $\bar{\phi}$

In [4], Wu et al. studied the PFC model with FCC ordering structure and presented a phase diagram which illustrated typical phase states (i.e., liquid, hex, fcc, and stripe) under different values of ϵ and $\bar{\phi}$. In this subsection, we numerically investigate the phase states by setting the corresponding parameters. The computational domain is $\Omega = [0, 32] \times [0, 32]$. The initial state is defined as $\phi(x, y, 0) = \phi + 0.01\text{rand}(x, y)$. We set $\Delta t = 0.1$, $h = 1/3$, and $\xi = 0.01$. The simulations are conducted until $t = 2000$. Fig. 5(a) shows the phase diagram which was adapted from [4]. For the liquid state, we use $(\epsilon, \bar{\phi}) = (0.1, -0.3)$ and display the final stage in (b). For the phase states with fcc, stripe, and hex, the parameters are $(\epsilon, \bar{\phi}) = (0.1, -0.1)$, $(0.2, -0.25)$, and $(0.2, 0)$, respectively. The corresponding results are shown in (b), (c), and (d). The present simulations are in good agreement with the phase diagram. As the decrease of magnitude of $\bar{\phi}$, the effect of nonlinear potential at early stage is weak. The linear terms lead to the formations of diffusion layers. With the growth of perturbation, the stripe patterns appear. From a macroscopic perspective, these stripe patterns probably approximate the growth striations on a crystal.

4.4. Crystallization with different crystallites

In the supercooled liquid, the small crystallites with different orientations will grow in time. Eventually, the crystal grains can occupy the whole domain and the different orientations generally lead to the formation of defects. In this simulation, we define $\Omega = [0, 256] \times [0, 256]$. The time step and space step are $\Delta t = 0.1$ and $h = 1$. We use $\epsilon = 0.25$ and $\xi = 0$. First, we compare the different dynamics driven by the PFC model with FCC ordering and BCC ordering. For the case with BCC ordering, we simply set $L_2 = 1$. At initial stage, the single crystallite is defined as

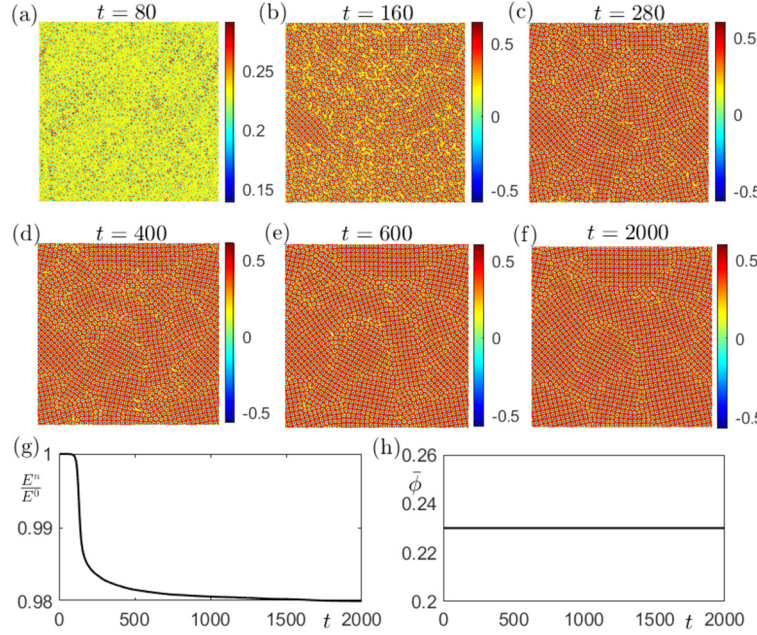


Fig. 3. Long-time simulation of phase transition with FCC ordering structure. Here, (a)-(f) displays the snapshots at different moments. The normalized energy and average concentration are shown in (g) and (h), respectively. (For interpretation of the colors in the figure(s), the reader is referred to the web version of this article.)

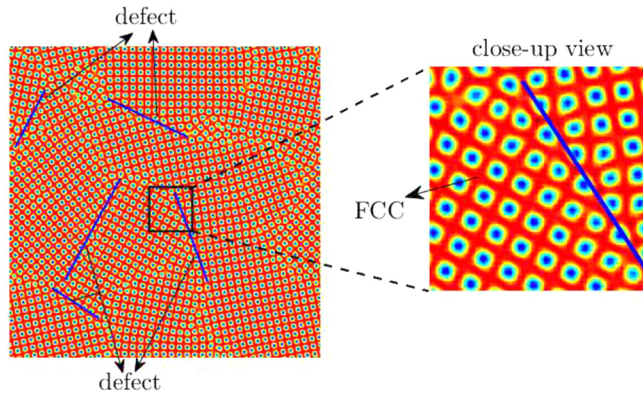


Fig. 4. Snapshot at $t = 2000$ and the local close-up view are shown. The blue lines represent the position of grain boundaries (defects).

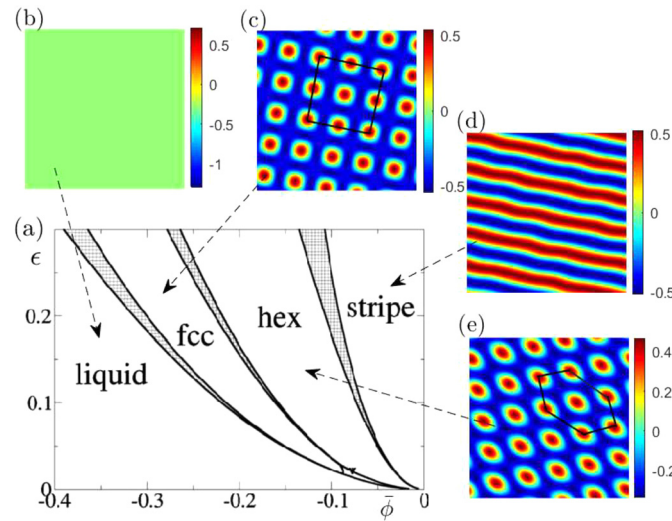


Fig. 5. Effects of ϵ and $\bar{\phi}$ on the phase state. Here, (a) is the phase diagram adapted from [4] with the permission of APS. From (b)-(e), the phase states with liquid, fcc, hex and stripe are shown.

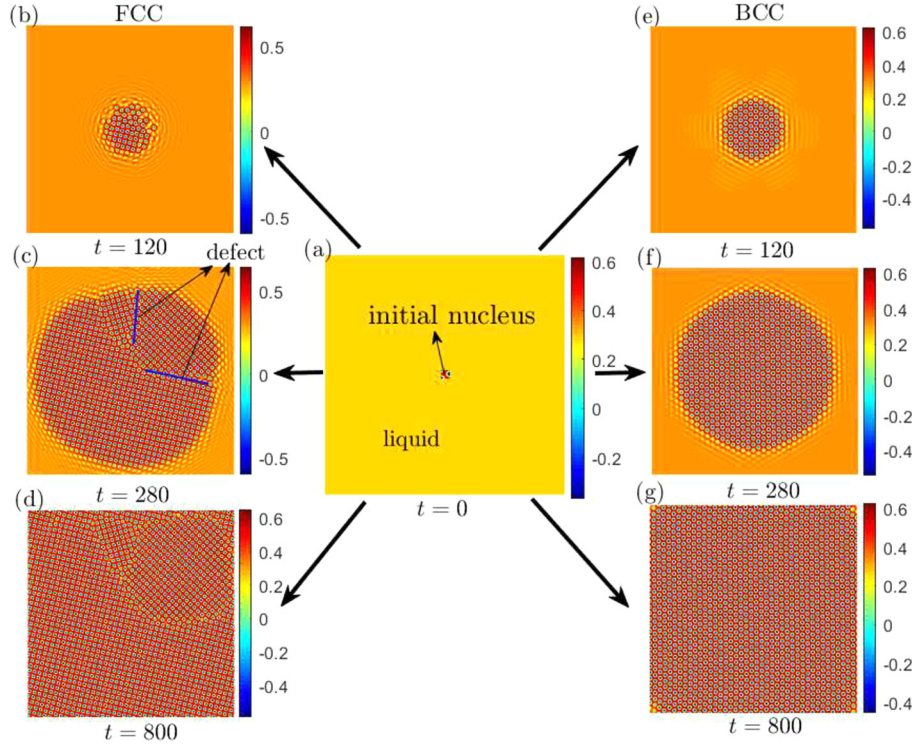


Fig. 6. Crystallization from a single crystallite. Here, (a) is the initial state. The results with FCC ordering and BCC ordering are shown in (b)-(d) and (e)-(g), respectively.

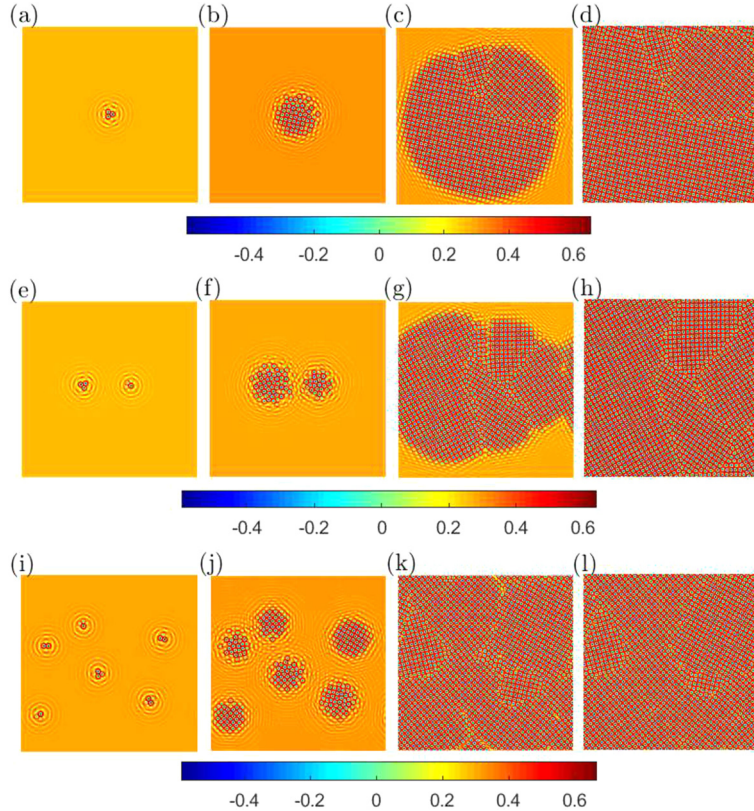


Fig. 7. Crystallization in the supercooled liquid. From the top to bottom, the first, second, and third rows show the results with single crystallite, two crystallites, and six crystallites, respectively. From the left to right, the snapshots in each row are at $t = 40, 120, 280$, and 800 .

$$\phi(x, y, 0) = 0.285 + 0.446 \left(\cos\left(\frac{0.66}{\sqrt{3}}y_l\right) \cos(0.66x_l) - 0.5 \cos\left(\frac{1.32}{\sqrt{3}}y_l\right) \right), \quad (26)$$

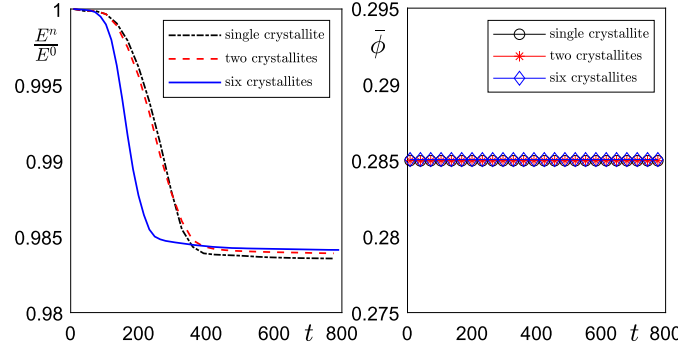


Fig. 8. Time evolutions of normalized energy curves (left) and average concentrations (right) with respect to single crystallite, two crystallites, and six crystallites.

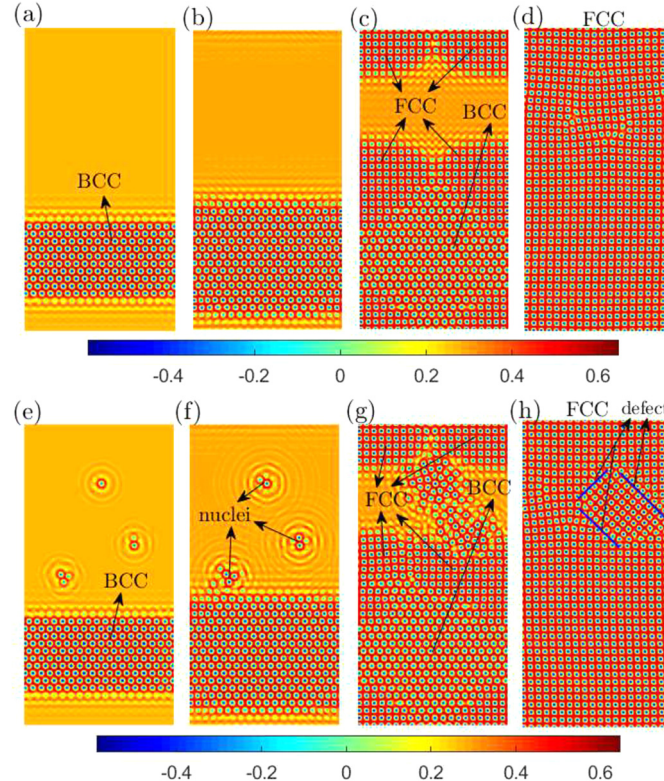


Fig. 9. Crystallization with mixed initial setting. Here, the top and bottom rows show the results under different initial conditions. With more perturbations, the grain boundaries (defects) can be observed in time.

where $x_l = x \sin \theta + y \cos \theta$ and $y_l = -x \cos \theta + y \sin \theta$. Here, we set $\theta = 0$. Fig. 6(a) shows the initial state. The results with FCC ordering and BCC ordering are shown in (b)-(d) and (e)-(g), respectively. It can be observed that the grain boundaries (defects) are not observed in the PFC model with BCC ordering.

Next, we simulate the multiple crystallites-driven crystallization. The computational domain and parameters are unchanged. From the top to bottom, the first, second, and third rows of Fig. 7 show the results with single crystallite, two crystallites, and six crystallites, respectively. For each initial crystallite, the orientation (i.e., θ) takes a different value. The results indicate that more defect structures appear with the increase of crystallite. In Fig. 8, we plot the normalized energy curves and average concentrations. It can be observed that the energy is non-increasing in time and the mass is conserved.

Finally, we investigate the crystallization with mixed initial setting in $\Omega = [0, 128] \times [0, 256]$. In the top row of Fig. 9, the results correspond to the following initial condition

$$\phi(x, y, 0) = 0.285 + 0.446 \left(\cos\left(\frac{\sqrt{3}}{2}x\right) \cos\left(\frac{y}{2}\right) - 0.5 \cos y \right), \text{ if } |y - 60| < 30,$$

and $\phi(x, y, 0) = 0.285$ in other regions. At early stage, many BCC ordering structures can be observed. With time evolution, these BCC structures are gradually transformed into the FCC ordering structures. The second row of Fig. 9 shows the results with respect to mixed initial setting, i.e., the above initial condition combining with three crystallites. Since the orientations of crystallites are different, the distinct grain boundaries (defects) are observed in time. Since ϕ represents the local density of crystal, the parameters for generating different patterns are symmetric about $\bar{\phi} = 0$ in Fig. 5. Therefore, the present parameters can lead to the formation of FCC ordering structure. Actually, the initial setting of the present simulation is the equilibrium state of BCC ordering structure. As reported in [4], the

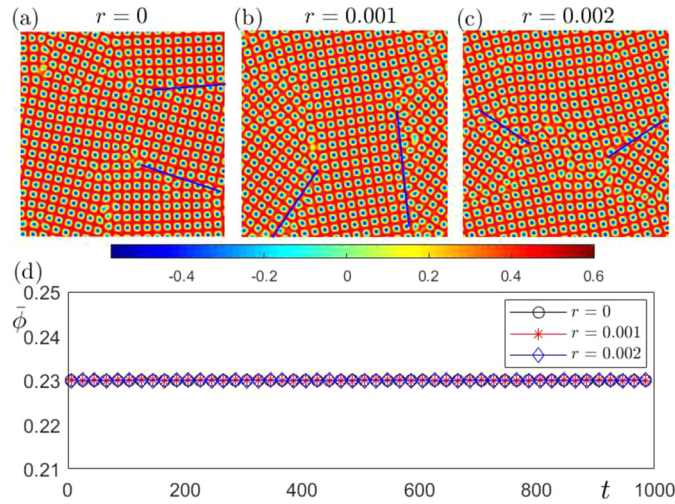


Fig. 10. Effect of r on the pattern formation. Here, (a)-(c) correspond to $r = 0$, 0.001, and 0.002. The evolutions of average concentrations are shown in (d).

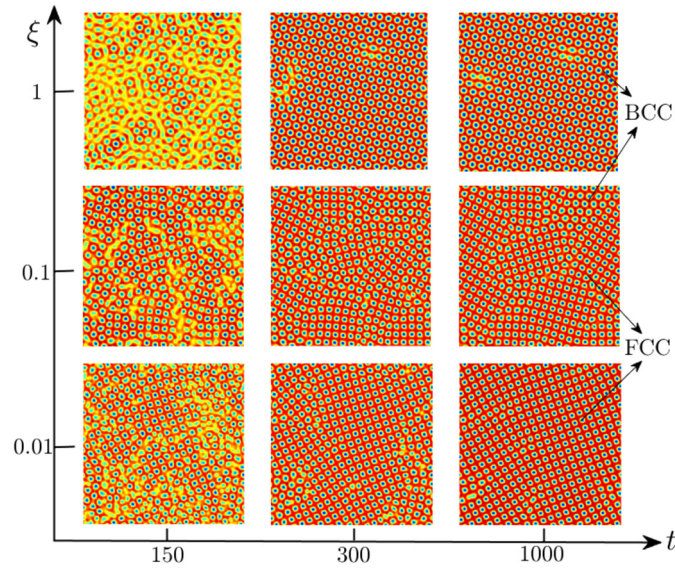


Fig. 11. Effect of ξ on the pattern formation. We let t and ξ be the horizontal and normal coordinates. The results with respect to different ξ and moments are shown.

similar energy structures of PFC models with BCC and FCC ordering structures usually bring similar evolutions at early stage. Therefore, we first observe that these BCC structures approximately keep the original patterns. With time evolution, the minimization of free energy with FCC ordering becomes dominant and leads to the transition from BCC ordering to FCC ordering. The thermodynamics is the main driving force of the whole process.

4.5. Effect of r

It is worth noting that the proposed model becomes the nonlocal AC-type PFC model with FCC ordering [39] if we set $r = 0$. When $r \neq 0$, the mass-conserved model contains the local effect. To show the effect of r on the pattern formation, we herein use $r = 0$, 0.001, and 0.002. The domain is defined as $\Omega = [0, 128] \times [0, 128]$. The initial condition is $\phi(x, y, 0) = 0.23 + 0.01\text{rand}(x, y)$. The parameters are $\Delta t = 0.1$, $h = 1$, $\epsilon = 0.195$, and $\xi = 0.01$. The snapshots at $t = 1000$ with respect to different r are shown in Fig. 10(a), (b), and (c). It can be observed that the nonlocal term obviously affects the positions of grain boundaries (defects). The evolutions of average concentrations are shown in Fig. 10(d). The results indicate that the local and the nonlocal models preserve the mass.

4.6. Effect of ξ

In the PFC model with FCC ordering structure, ξ is an important constant to scale the local atomic density. To investigate the effect of ξ on the pattern formation, we herein adopt the same initial setting and parameters in previous subsection and consider $\xi = 0.01$, 0.1, and 1. Let t and ξ be the horizontal and normal coordinates, Fig. 11 displays the numerical results with respect to different ξ and moments. As $\xi = 0.01$, the phase transition leads to the formation of FCC ordering structures. As we increase ξ to 0.1, the mixed patterns with FCC ordering structures and BCC ordering structures are observed. When $\xi = 1$ is used, we find that the evolutional dynamics at early stage is delayed. Moreover, only BCC ordering structures are left. The present simulations indicate that the value of ξ plays an essential role in generating the FCC or the BCC ordering structures.

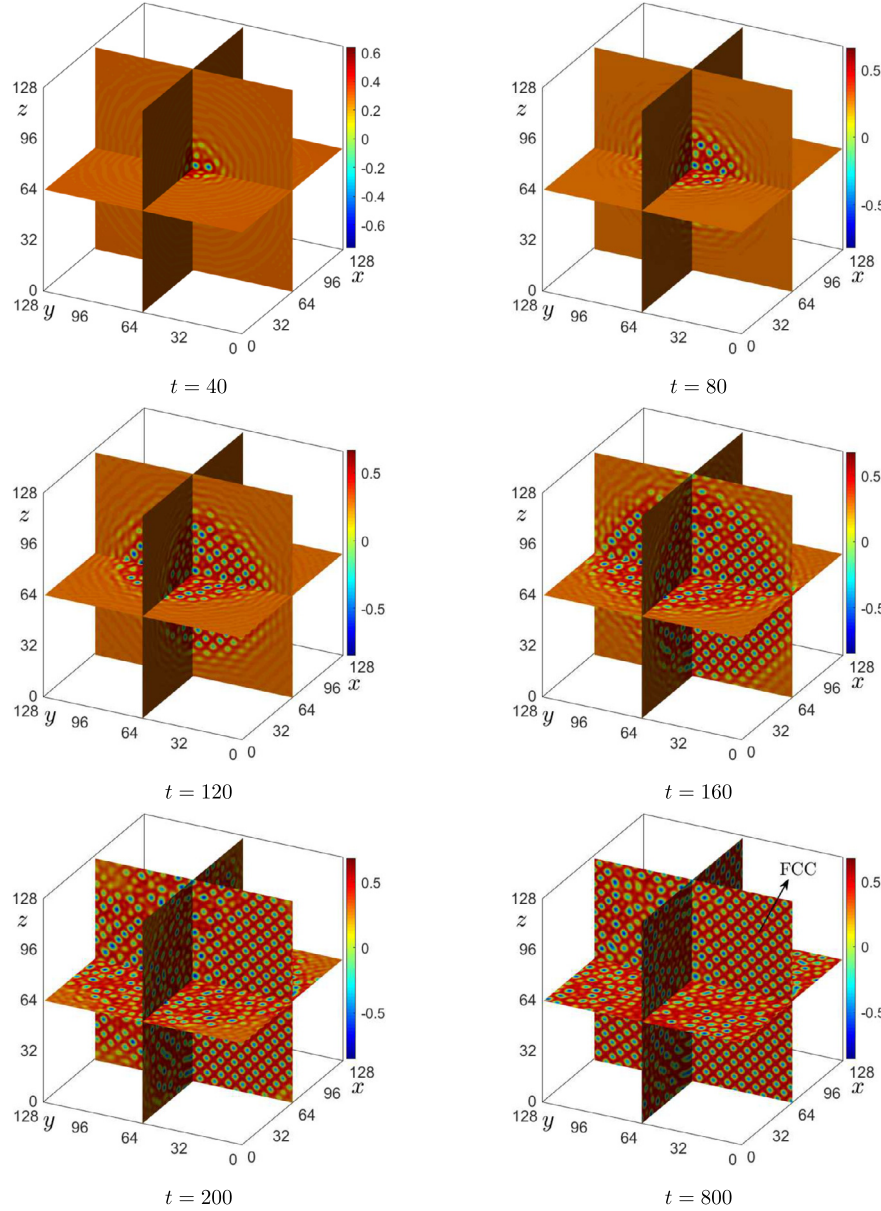


Fig. 12. Crystallization in 3D space. With time evolution, the FCC ordering structure can be observed. Under each figure, the computational moments are shown.

4.7. Crystallization in 3D space

Finally, we confirm the capability of our proposed method via the simulation of crystallization in 3D space. The domain is $\Omega = [0, 128] \times [0, 128] \times [0, 128]$. The parameters are set to be $h = 1$, $\Delta t = 0.1$, $r = 0$, $\epsilon = 0.25$, and $\xi = 0$. At initial stage, we define the following condition in a cubic cell $[54, 74] \times [54, 74] \times [54, 74]$

$$\begin{aligned} \phi(x, y, z, 0) = & 0.285 + 0.446(\cos(0.66x_l)\cos(0.38y_l) + \cos(0.66x_l)\cos(0.46z_l) + \cos(0.38y_l)\cos(0.46z_l) \\ & - 0.5\cos(0.38y_l)). \end{aligned} \quad (27)$$

In other regions, we set $\phi(x, y, z, 0) = 0.285$. Fig. 12 shows the snapshots of crystallization at different moments. With time evolution, the small crystallite grows and leads to the crystallization in nearby liquid. As we can observe, the FCC ordering structure appears. The MATLAB code of this 3D simulation is given in Appendix A.

5. Concluding remarks

In this work, we developed a simpler AC-type PFC model with FCC ordering structure with generalized mass constraint. The proposed model not only has lower-order spatial derivative but also analytically preserved the total mass. The local effect was reflected by a space-time dependent Lagrange multiplier. To solve the proposed in an efficient and accurate manner, the third-order time-accurate scheme based IMEX RK approach was proposed. In space, the Fourier spectral method was used. In each time step, we only needed to successively

solve four linear elliptic type equations with constant coefficients. The discrete mass conservation of our proposed scheme has been analytically estimated. The numerical simulations indicated the desired accuracy, efficiency, and capability.

Declaration of competing interest

The authors declare that they have no known competing financial interests or personal relationships that could have appeared to influence the work reported in this paper.

Data availability

Data will be made available on request.

Acknowledgement

J. Yang is supported by the National Natural Science Foundation of China (No. 12201657), the China Postdoctoral Science Foundation (No. 2022M713639), and the 2022 International Postdoctoral Exchange Fellowship Program (Talent-Introduction Program) (No. YJ20220221). The work of Z. Tan is supported by the National Nature Science Foundation of China (11971502), Guangdong Natural Science Foundation (2022A1515010426), Guangdong Province Key Laboratory of Computational Science at the Sun Yat-sen University (2020B1212060032), and Key-Area Research and Development Program of Guangdong Province (2021B0101190003). The authors thank the reviewers for the constructive comments on the revision of this work. Moreover, the corresponding author appreciates Professor Hyun Geun Lee at Kwangwoon University for her preliminary and valuable research on the IMEX RK algorithm for the L^2 -gradient flow-based PFC model.

Appendix A

The following MATLAB codes are used to simulate phase transition with random initial state in subsection 4.2 and 3D crystallization in subsection 4.7. After minor modifications, the codes can be easily extended for other simulations in this paper.

```
%2D code for phase transition
Lx = 256; xleft = 0; xright = xleft+Lx;
Ly = 256; yleft = 0; yright = yleft+Ly;
Mx = 256; dx = Lx/Mx; x = xleft+(0:Mx-1)*dx;
My = 256; dy = Ly/My; y = yleft+(0:My-1)*dy;
xix = 2*pi*[0:Mx/2:-1-Mx/2:-1]/Lx;
xiy = 2*pi*[0:My/2:-1-My/2:-1]/Ly;
[kx,ky] = ndgrid(xix,xiy);
dt = 0.1;
h = dx;
R = 0.01*(2*rand(Mx,My)-1); ophi = 0.23+(R-mean(mean(R)));
epsilon = 0.195; g = 0; r = 0.0; s = 2; T = 2000; order = 3;
qq = sqrt(2); rr = 0.01;
kp = -(s-(2*qq^4+2*qq^2+2*rr^2)*(kx.^2+ky.^2)+...
(qq^4+4*qq^2+1+rr^2)*(kx.^2+ky.^2).^2-...
(2*qq^2+2)*(kx.^2+ky.^2).^(3+(kx.^2+ky.^2).^4));
switch order
case 1
MI = 1; ME = MI;
case 2
gamma = (2-sqrt(2))/2; lap = 1-1/(2*gamma);
MI = [gamma 0; 1-gamma gamma]; ME = [gamma 0; lap 1-lap];
case 3
MI = [1/2 0 0 0; 1/6 1/2 0 0; -1/2 1/2 1/2 0; 3/2 -3/2 1/2 1/2];
ME = [1/2 0 0 0; 11/18 1/18 0 0; 5/6 -5/6 1/2 0; 1/4 7/4 3/4 -7/4];
end
ns = length(MI);
for n=1:round(T/dt)
ophi_hat = fft2(ophi);
phis = zeros(Mx,My,ns); q = zeros(Mx,My,ns);
for i = 1:ns
Phip = ophi.^3-epsilon*ophi+(qq^4+rr^2)*ophi;
Phir = (1/4*ophi.^4-epsilon/2*ophi.^2+(qq^4+rr^2)/2*ophi.^2).^r;
beta = sum(sum(Phip))/sum(sum(Phir));
q(:,:,i) = -(Phip-s*ophi)+Phir*beta;
IM = 0; EX = ME(i,i)*q(:,:,i);

```

```

for j=1:i-1
IM = IM + MI(i,j)*phis(:,:,j);
EX = EX + ME(i,j)*q(:,:,j);
end
phis(:,:,i) = (ophi_hat+dt*(kp.*IM+fft2(EX)))./(1-MI(i,i)*dt*kp);
ophi = real(ifft2(phis(:,:,i)));
end
if (mod(n,40)==0 )
figure(1);clf;
[xx,yy] = ndgrid(x,y); pcolor(xx,yy,ophi); shading interp;
colormap jet; axis image off;
end
end

```

```

%3D code for crystallization
clear;
Lx = 128; xleft = 0; xright = xleft+Lx;
Ly = 128; yleft = 0; yright = yleft+Ly;
Lz = 128; zleft = 0; zright = zleft+Lz;
Mx = 128; dx = Lx/Mx; x = xleft+(0:Mx-1)*dx;
My = 128; dy = Ly/My; y = yleft+(0:My-1)*dy;
Mz = 128; dz = Lz/Mz; z = zleft+(0:Mz-1)*dz;
[xx,yy,zz]=meshgrid(x,y,z);
xix = 2*pi*[0:Mx/2:-1:-Mx/2:-1]/Lx;
xiy = 2*pi*[0:My/2:-1:-My/2:-1]/Ly;
xiz = 2*pi*[0:Mz/2:-1:-Mz/2:-1]/Lz;
[kx,ky,kz] = ndgrid(xix,xiy,xiz);
dt = 0.1;
h = dx;
epsilon = 0.25; g = 0; r = 0.0; s = 2; T = 800; order = 3;
qq = sqrt(2); rr = 0.0;
kp = -(s-(2*qq^4+2*qq^2+2*rr^2)*(kx.^2+ky.^2+kz.^2)...
+ (qq^4+4*qq^2+1+rr^2)*(kx.^2+ky.^2+kz.^2).^2 ...
- (2*qq^2+2)*(kx.^2+ky.^2+kz.^2).^3+(kx.^2+ky.^2+kz.^2).^4);
for i = 1:Mx
    for j = 1:My
        for k = 1:Mz
            theta = 0;
            ophi(i,j,k) = 0.285;
            theta = 0.0;
            if( x(i)> 54 && x(i) < 74 && y(j) > 54 && y(j) < 74&& z(k) > 54 && z(k) < 74)
                xl(i,j,k) = x(i);
                yl(i,j,k) = y(j)*cos(theta)-z(k)*sin(theta);
                zl(i,j,k) = y(j)*sin(theta) + z(k)*cos(theta);
                ophi(i,j,k) = 0.285+0.446*( cos(0.66*xl(i,j,k))*cos(0.38*yl(i,j,k))...
                + cos(0.66*xl(i,j,k))*cos(0.46*zl(i,j,k))...
                + cos(0.38*yl(i,j,k))*cos(0.46*zl(i,j,k)) - 0.5*cos(0.38*yl(i,j,k)) );
            end
        end
    end
end
figure(1);
slice(xx,yy,zz,ophi,64,64,64); grid off;
view(-63,25);
camlight left; lighting phong;
shading interp;
colormap jet;
daspect([1 1 1]);
switch order
case 1
MI = 1; ME = MI;

```

```

case 2
gamma = (2-sqrt(2))/2; lap = 1-1/(2*gamma);
MI = [gamma 0; 1-gamma gamma]; ME = [gamma 0; lap 1-lap];
case 3
MI = [1/2 0 0 0; 1/6 1/2 0 0; -1/2 1/2 1/2 0; 3/2 -3/2 1/2 1/2];
ME = [1/2 0 0 0; 11/18 1/18 0 0; 5/6 -5/6 1/2 0; 1/4 7/4 3/4 -7/4];
end
ns = length(MI);
cot = 1;
for n=1:round(T/dt)
ophi_hat = fftn(ophi);
phis = zeros(Mx,My,Mz,ns); q = zeros(Mx,My,Mz,ns);
for i = 1:ns
Phip = ophi.^3-epsilon*ophi+(qq^4+rr^2)*ophi;
Phir = (1/4*ophi.^4-epsilon/2*ophi.^2+(qq^4+rr^2)/2*ophi.^2).^r;
beta = sum(sum(Phip))/sum(sum(Phir));
q(:,:,:,:i) = -(Phip-s*ophi)+Phir*beta;
IM = 0; EX = ME(i,i)*q(:,:,:,:i);
for j=1:i-1
IM = IM + MI(i,j)*phis(:,:,:,:j);
EX = EX + ME(i,j)*q(:,:,:,:j);
end
phis(:,:,:,:i) = (ophi_hat+dt*(kp.*IM+fftn(EX)))./(1-MI(i,i)*dt*kp);
ophi = real(ifftn(phis(:,:,:,:i)));
end
if (mod(n,200)==0 )
cot = cot + 1;
figure(cot);
slice(xx,yy,zz,ophi,64,64,64); grid off;
view(-63,25);
camlight left; lighting phong;
shading interp;
colormap jet;
daspect([1 1 1]);
end
end

```

References

- [1] Z. Guan, V. Heinonen, J. Lowengrub, C. Wang, S.M. Wise, *J. Comput. Phys.* 321 (2016) 1026–1054.
- [2] Y. Li, C. Luo, B. Xia, J. Kim, *Appl. Math. Model.* 67 (2019) 477–490.
- [3] M. Dehghan, V. Mohammadi, *Comput. Methods Appl. Mech. Eng.* 298 (2016) 453–484.
- [4] K-A. Wu, A. Adland, A. Karma, *Phys. Rev. E* 81 (2010) 061601.
- [5] M. Wang, Q. Huang, C. Wang, *J. Sci. Comput.* 88 (2021) 33.
- [6] J. Yang, J. Kim, *J. Comput. Phys.* 471 (2022) 111652.
- [7] Q. Li, X. Yang, L. Mei, *Commun. Math. Sci.* 19 (2) (2021) 355–381.
- [8] K. Jiang, P. Zhang, *J. Comput. Phys.* 256 (2014) 428–440.
- [9] J. Yin, K. Jiang, A-C. Shi, P. Zhang, L. Zhang, *Proc. Natl. Acad. Sci. USA* 118 (49) (2021) e2106230118.
- [10] G. Zhu, J. Kou, S. Sun, J. Yao, A. Li, *Comput. Phys. Commun.* 233 (2018) 67–77.
- [11] Y. Li, Q. Xia, S. Yoon, C. Lee, B. Lu, J. Kim, *Comput. Phys. Commun.* 264 (2021) 107956.
- [12] A. Zhang, J. Du, Z. Guo, Q. Wang, S. Xiong, *Comput. Phys. Commun.* 267 (2021) 108042.
- [13] Q. Li, L. Mei, *Comput. Phys. Commun.* 260 (2021) 107290.
- [14] J. Yang, J. Wang, Z. Tan, J. Kim, *Comput. Phys. Commun.* 282 (2023) 108558.
- [15] K.R. Elder, M. Katakowski, M. Haataja, M. Grant, *Phys. Rev. E* 88 (24) (2002) 245701.
- [16] S.M. Wise, C. Wang, J.S. Lowengrub, *SIAM J. Numer. Anal.* 47 (3) (2009) 2269–2288.
- [17] Z. Hu, S.M. Wise, C. Wang, J.S. Lowengrub, *J. Comput. Phys.* 228 (15) (2009) 5323–5339.
- [18] C. Wang, S.M. Wise, *SIAM J. Numer. Anal.* 49 (3) (2011) 945–969.
- [19] A. Baskaran, Z. Hu, J. Lowengrub, C. Wang, S. Wise, P. Zhou, *J. Comput. Phys.* 250 (2013) 270–292.
- [20] A. Baskaran, J. Lowengrub, C. Wang, S. Wise, *SIAM J. Numer. Anal.* 51 (2013) 2851–2873.
- [21] K. Cheng, C. Wang, S. Wise, *Commun. Comput. Phys.* 26 (2019) 1335–1364.
- [22] L. Dong, W. Feng, C. Wang, S.M. Wise, Z. Zhang, *Comput. Math. Appl.* 75 (6) (2018) 1912–1928.
- [23] H.G. Lee, J. Shin, J-Y. Lee, *J. Comput. Phys.* 299 (2015) 82–91.
- [24] H.G. Lee, J. Shin, J-Y. Lee, *Comput. Methods Appl. Mech. Eng.* 321 (2017) 1–17.
- [25] B. Xia, C. Mei, Q. Yu, Y. Li, *Comput. Methods Appl. Mech. Eng.* 363 (2020) 112795.
- [26] Y. Li, J. Kim, *Comput. Methods Appl. Mech. Eng.* 319 (2017) 194–216.
- [27] Q. Li, L. Mei, B. You, *Appl. Numer. Math.* 134 (2018) 46–65.
- [28] Z. Liu, X. Li, *Numer. Algorithms* 85 (2020) 107–132.
- [29] P.C. Hohenberg, J.B. Swift, *Phys. Rev. A* 46 (1992) 4773–4785.
- [30] J. Su, W. Fang, Q. Yu, Y. Li, *Comput. Appl. Math.* 38 (2019) 54.
- [31] H.G. Lee, *Comput. Methods Appl. Mech. Eng.* 343 (2019) 40–51.
- [32] J. Yang, J. Kim, *J. Eng. Math.* 128 (2021) 21.

- [33] H.G. Lee, *J. Comput. Appl. Math.* 375 (2020) 112815.
- [34] H.G. Lee, *Mathematics* 8 (2020) 1502.
- [35] J. Yang, Z. Tan, J. Kim, *Comput. Math. Appl.* 102 (2021) 160–174.
- [36] Q. Li, L. Mei, *J. Sci. Comput.* 88 (3) (2021) 60.
- [37] X.D. Xu, P. Liu, S. Guo, A. Hirata, T. Fujita, T.G. Nieh, C.T. Liu, M.W. Chen, *Acta Mater.* 84 (2015) 145–152.
- [38] J. Zhang, X. Yang, *Appl. Numer. Math.* 146 (2019) 13–37.
- [39] Q. Li, N. Cui, S. Zheng, L. Mei, *Appl. Math. Lett.* 132 (2022) 108211.
- [40] J. Kim, S. Lee, Y. Choi, *Int. J. Eng. Sci.* 84 (2017) 11–17.
- [41] D. Lee, J. Kim, *Math. Comput. Simul.* 119 (2016) 35–56.
- [42] Y. Li, D. Jeong, H. Kim, C. Lee, J. Kim, *Comput. Math. Appl.* 77 (2019) 311–322.
- [43] S. Yoon, D. Jeong, C. Lee, H. Kim, S. Kim, H.G. Lee, J. Kim, *Mathematics* 8 (2020) 1385.
- [44] H.G. Lee, *Comput. Math. Appl.* 72 (2016) 620–631.